Quantifying the impact of dispersion, acidity and porosity of Mo/HZSM-5 on the performance in methane dehydroaromatization

Vollmer, Ina; Mondal, Amantrita; Yarulina, Irina; Abou-Hamad, Edy; Kapteijn, Freek; Gascon, Jorge

DOI
10.1016/j.apcata.2019.01.022

Publication date
2019

Document Version
Final published version

Published in
Applied Catalysis A: General

Applied Catalysis A, General 574 (2019) 144–150

Contents lists available at ScienceDirect

Applied Catalysis A, General

journal homepage: www.elsevier.com/locate/apcata

Quantifying the impact of dispersion, acidity and porosity of Mo/HZSM-5 on the performance in methane dehydroaromatization

Ina Vollmer[a], Amantrita Mondal[a], Irina Yarulina[b], Edy Abou-Hamad[c], Freek Kapteijn[a,*], Jorge Gascon[a,b]

[a] Catalysis Engineering, Chemical Engineering Department Delft University of Technology, Van der Maasweg 9, 2629 HZ Delft, the Netherlands
[b] King Abdullah University of Science and Technology, KAUST Catalysis Center, Advanced Catalytic Materials, Thuwal 23955, Saudi Arabia
[c] King Abdullah University of Science and Technology, Core Labs, Thuwal 23955, Saudi Arabia

ARTICLE INFO

Keywords:
Methane dehydroaromatization
Mo/HZSM-5
CVD
Sublimation
Py IR
UV–vis
XPS
XRD
N_2 adsorption

ABSTRACT

The catalytic performance of the bifunctional catalyst Mo/HZSM-5 for methane dehydroaromatization (MDA) depends on the Mo dispersion and on zeolite acidity. Here we separately quantify the effect of dispersion and the effect of acidity on aromatic yields and coke selectivity. Also, the effect of porosity on the same is quantitatively assessed. For that, a suite of 17 samples with varying Mo dispersion were synthesized by means of several methods, including chemical vapor deposition with $MoCl_5$, MoO_2Cl_2 and $Mo(CO)_6$ as precursors and the conventional methods, incipient wetness impregnation and solid ion exchange. These catalysts were characterized with pyridine IR-spectroscopy, XPS, UV–vis spectroscopy, N_2 adsorption, XRD, TGA and ^{27}Al MAS NMR. The combined results yielded a measure of how much Mo is anchored to the zeolite as well-defined cationic species and how much is present as bigger clusters on the outer surface of the zeolite. Through relating these characterization results to the catalytic behavior of the catalysts, it was found that the maximum instantaneous benzene and naphthalene yields as well as the integral selectivities during methane dehydroaromatization linearly increase with the amount of Mo present as mono- or dimeric species. At the same time, the selectivity to coke increases with the amount of Mo present as bigger clusters or nanoparticles on the outer surface of the zeolite. The number of Mo cationic sites is the most important factor determining the activity of Mo/HZSM-5 for low loadings of Mo. But at higher loadings, the high rate of aromatics formation requires an easily accessible pore structure as well.

1. Introduction

Converting methane to aromatics, an important building block of many consumer goods and pharmaceuticals, is desirable because this small and very stable hydrocarbon is highly available [1]. For valorizing methane, steam reforming combined with Fischer-Tropsch synthesis is one of the indirect routes already applied industrially. However, there is great commercial interest in directly converting methane to aromatics. A process that can achieve this without the addition of oxidants is preferred, as the production of CO and CO_2 can be avoided and carbon efficiency is superior in that case. Thermodynamically, however, the direct non-oxidative conversion of methane to benzene is limited, with values for $\Delta G_r^o = +104\,\mathrm{kcal\,mol^{-1}}$ and $\Delta H_r^0 = +127\,\mathrm{kcal\,mol^{-1}}$ [2–4]. Thus, considerable conversion of methane and yields of benzene (7.8–21.5 $\mathrm{mol_C\%}$) can only be achieved at high temperature, practically between 923 and 1073 K, while coke formation is much less limited at these temperatures. This usually leads to fast deactivation of the catalyst. Catalyst deactivation and regeneration is the biggest concern when designing a catalyst for the methane dehydroaromatization (MDA) reaction. The best performing catalysts for this system, Mo/HZSM-5 and Mo/MCM-22 [5–9] almost reach the thermodynamic limit in the beginning of the reaction operation, but their activity immediately decreases once it reached its maximum [2,3].

The most important aspects that were found to influence catalytic activity and stability were Mo dispersion, acidity [10–14] and porosity [15,16] of the zeolite support. The catalyst is believed to be most active when Mo is anchored to the framework Al inside the pores of the zeolite via oxygen bridges, (partially) replacing the proton of the Brønsted acid site (BAS) [17–19]. Mo was found to be either mono- [17] or dimeric

* Corresponding author.
E-mail address: f.kapteijn@tudelft.nl (F. Kapteijn).

https://doi.org/10.1016/j.apcata.2019.01.022
Received 8 November 2018; Received in revised form 12 January 2019; Accepted 27 January 2019
Available online 29 January 2019
0926-860X/

[20] when anchoring to the zeolite. The anchoring capacity is therefore limited by the concentration of framework Al and its distribution in the framework [21]. Several studies reported optimal activity per Mo atom for Mo loadings between 2 and 4 wt.%, corresponding to Mo/Al ratios far below 1 [10,22–24]. The Mo that does not anchor to the framework is left as polymeric structures inside the pores or as nanoparticles on the outer surface of the zeolite, which is hard to avoid and believed to be the main cause of coking [10,17,22–24]. Some approaches exist to minimize the presence of Mo nanoparticles on the outer surface of the zeolite: silanation of the external surface of the zeolite prior to introduction of Mo [13] or adding small amounts of ammonia to the impregnation solution [25]. X-ray photoelectron spectroscopy (XPS) can be used to detect Mo on the outer surface of the zeolite, as it is a surface sensitive technique, while UV-Raman and UV–vis spectroscopy (UV–vis) yield information about the Mo state in the whole particle [10,26]. Tian et al. related the electronic edge energy (E_g) of the ligand-to-metal charge transfer transitions of Mo cations determined by UV–vis to the number of bridging Mo—O—Mo and thereby developed a way to determine the average cluster size of Mo [27]. Further, the dispersion of Mo can be probed indirectly by probing the acidity of the catalyst using H/D exchange [18,20,28], ^{1}H NMR [29,30], ^{27}Al MAS NMR [31,32], NH_3-TPD [10,15,33,34] or probing adsorbed molecules by IR-spectroscopy [35,36] (Py IR). The more the BAS concentration decreases compared to the pristine zeolite, the higher is the achieved dispersion. At the same time, it has to be carefully assessed that the BAS decrease is not partly due to destruction of the zeolite by extraction of the framework Al (FAl) during introduction of Mo. This is best achieved by ^{27}Al MAS NMR.

Mo/HZSM-5 is most commonly prepared by incipient wetness impregnation (IWI), where an aqueous solution containing $(NH_4)_6Mo_7O_{24}$ (ammonium heptamolybdate, AHM) with a volume to just fill the pores of the zeolite is added dropwise to the dry zeolite. Mo is present as $Mo_7O_{24}{}^{6-}$ in the impregnation solution, an ion that does not fit into the pores of the zeolite and remains at the outer surface of the particle. Only upon increasing the temperature MoO_3 moieties can form in air, which are able to migrate into the pore channels of the zeolite and anchor there [30]. This calcination step is performed with low heating rates (0.5–2 K/min) to avoid fast expansion of the liquid in the zeolite pores, which would impair their integrity and to facilitate migration of Mo, while avoiding agglomeration. The final temperature applied is between 773 and 973 K, where 873 K was found to lead to good dispersion of Mo, while maintaining decent integrity of the zeolite structure and limiting the extraction of framework Al to form Al_2MoO_4, which is catalytically inactive [37,38]. In some publications MoO_3 powder is mixed with the zeolite directly and then calcined. This is usually referred to as solid ion exchange (SIE) [39,40]. It is clear that Mo has to form some volatile or mobile species that can migrate into the pores of the zeolite in order to achieve good dispersion and with that a good catalytic activity. MoO_3 however has a very high melting point of 1068 K and was observed to start to evaporate at around 973 K in inert atmosphere [41]. Therefore, here we also employ another synthesis approach using Mo precursors with very low melting points in combination with chemical vapor deposition (CVD). Two chloride precursors, $MoCl_5$ (m.p. 467 K) and MoO_2Cl_2 (m.p. 448 K) as well as $Mo(CO)_6$ (m.p. 423 K) are explored. Here, we compare the Mo dispersion achieved with the different synthesis techniques and relate it to benzene and naphthalene selectivities and yields as well as coke selectivity. Dispersion of Mo is determined by a combination of XPS, pyridine IR-spectroscopy, UV–vis spectroscopy and ^{27}Al MAS NMR. Using N_2 adsorption, the role of the porosity of the as-synthesized catalysts is assessed on catalytic performance. From this we determine the most important parameters determining the performance of Mo/HZSM-5 for MDA and how that can be influenced by the synthesis.

2. Experimental

2.1. Catalyst synthesis

Mo was introduced into the H-form of a commercial HZSM-5 zeolite (PQCorporation, CBV 5020E) with Si/Al = 24 (denoted **HZ**) using IWI, SIE or CVD. Samples are denoted as ***y*MoHZ-*x***, where ***y*** denotes the Mo/Al ratio and ***x*** the synthesis method. Catalysts were prepared with Mo/Al = 0.3 and 1. If a precursor other than $MoCl_5$ is used for the synthesis, this is specifically indicated. The synthesis methods are described in detail in the Supplementary information.

2.2. Catalyst characterization

Pyridine transmission FTIR spectroscopy was performed on a Nicolet 6700 spectrometer with a MCT/B detector. A 10 mm wafer using 50 mg sample is pressed using 4.29 bar. The sample was first activated in vacuum at 400 °C for 16 h to remove adsorbed species. After activation, the pyridine gas was fed to the pellets until saturated and further evacuated at 160 °C for 2 h. Spectra were recorded in 1000–4000 cm^{-1} range at 4 cm^{-1} resolution and co-addition of 128 scans. The spectra shown represent the subtraction result of the spectra collected before adsorption of pyridine from the one taken afterwards. All spectra were normalized by the framework absorbance at 1873 cm^{-1}. The decrease in peak area characteristic for Brønsted acidity (BAS) at 1455 cm^{-1} is expressed by Eq. (1), where A represent the area of the absorbance with a certain vibration of either the catalyst containing Mo or the bare zeolite.

$$(Mo/Al)_{Py\ FTIR} = 1 - \left(\frac{A_{1546cm^{-1},sample}}{A_{1546cm^{-1},\ bare\ zeolite}}\right) \quad (1)$$

$(Mo/Al)_{Py\ FTIR}$ is a measure for how many BAS protons got replaced by Mo. The increase in Lewis acid sites (LASs) with respect to the bare zeolite due to the formation of Mo cations is expressed by Eq. (2).

$$LAS_{extra} = A_{1455cm^{-1},sample} - A_{1455cm^{-1},\ bare\ zeolite} \quad (2)$$

The UV–vis diffuse reflectance spectra (UV–vis-DRS) were collected on a Perkin–Elmer Lambda 900 spectrophotometer equipped with an integrating sphere ("Labsphere") in the 200–800 nm range. The bare zeolite was used as a white standard. Before measurement, the samples were degassed at 400 °C under dynamic vacuum for 12 h and then transferred to the sample holders in the glovebox. The absorption intensity is expressed by the Schuster-Kubelka-Munk equation (Eq. (3)).

$$F(R_\infty) = (1 - R_\infty)^2/2R_\infty \quad (3)$$

The edge energy (Eg) was determined by fitting a straight line to $(F(R_\infty)h\nu)^2$ plotted against the incident photon energy $h\nu$ in the low energy rise region [27].

Chemical composition of the samples in terms of Mo, and Al content was measured by digestion of approximately 50 mg sample in 4.5 ml 30% HCl + 1.5 ml 65% HNO_3 + 0.2 ml 40% HF using a microwave. The digestion time in the microwave was 60 min at 1000 W for 8 samples and 1300 W for 14 samples. After digestion, the samples were diluted to 50 ml with MQ and analysed with ICP-OES on a PerkinElmer Optima 5300 (torch:Si + saffire injector). For Na a PerkinElmer AAS Modell AAnalyst 200 was used.

X-ray photoelectron spectroscopy (XPS) analysis was performed in order to identify any agglomeration of Mo on the zeolite surface. A Thermo Scientific K-alpha spectrometer equipped with a monochromatic Al $K\alpha$ X-ray source and a 180° double-focusing hemispherical analyzer with a 128-2 channel detector was used. Measurements were performed at ambient temperature and chamber pressure of about 10^{-8}

mbar. The spot size was 400 mm. A flood gun was always used for charge compensation. The spectra were analyzed and processed by using Thermo Avantage v5.903 software (Thermo Fisher Scientific). Smart background (derived from the Shirley background) was used over the peak width. $(Mo/Al)_{XPS}$ was determined by quantifying the amount of Mo and Al from the XPS measurement as an average of two measurement points.

Catalytic testing was performed in a quartz reactor tube with an inner diameter of 6 mm, using 500 mg catalyst pelletized and sieved to 212–355 µm. A weight hourly space velocity (WHSV) of 1.21 h^{-1} (based only on methane flow) and a reaction temperature of 973 K was applied in all tests. Product analysis was achieved on an Interscience Trace GC with one TCD and two FIDs. A mixture 5% N_2 in CH_4 was fed to the reactor, where N_2 was used as an internal standard according to Eq. (4), where $A_{i,in}$ ($i = CH_4$ *or* N_2), the integrated peak area from the GC analysis is determined from three initial GC calibration injections before increasing the temperature for each run. The reactor was brought to reaction temperature under the same flow with a heating rate of 10 °C/min. Product yields were calculated according to Eq. (5), where F_n denotes the molar flow of molecule n, the number of carbons and y the number of hydrogens in a product molecule. The integral selectivity to each gaseous product i over the whole time on stream (TOS) is obtained using Eq. (6), where the number of the GC injection is denoted by j. Coke selectivity over the whole TOS calculated with Eq. (7).

$$X_{CH_4} = \frac{\left(\frac{A_{CH_4,in}}{A_{N_2,in}}\right) - \left(\frac{A_{CH_4,out}}{A_{N_2,out}}\right)}{\frac{A_{CH_4,in}}{A_{N_2,in}}} * 100\% \quad (4)$$

$$Y_i\,[mol\%] = \frac{F_{C_xH_y,out}}{F_{CH_4,in}} * x * 100\%, \quad i = product, \; C_xH_y \quad (5)$$

$$\sum_{TOS} S_i\,[mol\%] = \frac{\sum_j Y_i}{\sum_j X_{CH_4}} * 100\%, \quad j = GC\ injection\# \quad (6)$$

$$\sum_{TOS} S_{coke}\,[mol\%] = \sum_j X_{CH_4} - \sum_i \sum_{TOS} S_i \quad (7)$$

Samples of spent catalysts were analysed for porosity by N_2 adsorption and their coke content by thermogravimetric analysis (TGA, heating in air at 10 K/min, see section A5.7 in the SI).

3. Results

3.1. Effect of Mo loading

17 catalysts were prepared using several CVD methods found in literature as well as SIE and IWI. Three different precursors, $MoCl_5$, MoO_2Cl_2 and $Mo(CO)_6$ were used for CVD, while MoO_3 and $MoCl_5$ were tested for SIE and AHM for IWI. A detailed description and discussion of the synthesis methods and the catalytic performance achieved can be found in the Supplementary information sections A1–A3. While a better dispersion was achieved with CVD compared to IWI it also has to be noted that the synthesis was hard to reproduce and more consistent results were obtained with IWI.

Samples with two different loadings of Mo were prepared with Mo/Al = 0.3 and 1.0. The high loading corresponds to the theoretical limit of Mo incorporation, because each Al can theoretically anchor one Mo. This high loading was used to test how well the different synthesis methods perform, because it is hard to disperse Mo at the limit of how much Mo can be anchored. Generally, a better dispersion is achieved for Mo/Al = 0.3 as is evident from XPS as well as UV–vis (vide infra). The integrity of the zeolite is also less impaired by the synthesis method for Mo/Al = 0.3 compared to when the catalysts are prepared with Mo/Al = 1. This is concluded from the N_2 adsorption isotherms, XRD and ^{27}Al MAS NMR. For Mo/Al = 0.3, the N_2 adsorption isotherms (Fig. S8a) retain the same shape as the isotherm for the bare zeolite, while for catalysts prepared with Mo/Al = 1 a decrease in BET surface area is observed accompanied with, in some cases, increased mesoporosity (Fig. S8b). XRD patterns (Fig. S9) also show a more significant decrease in crystallinity for Mo/Al = 1 than for Mo/Al = 0.3. The diffraction peaks characteristic for MoO_3 are observed for more catalysts with Mo/Al = 1 than for Mo/Al = 0.3 showing that there is a higher chance of Mo agglomeration for high Mo loadings. ^{27}Al MAS NMR (Fig. S10) shows that some samples with Mo/Al = 1 experienced significant extraction of framework Al, while only moderate extraction is observed for Mo/Al = 0.3. Both EFAl as well as $Al_2(MoO_4)_3$ are observed especially for Mo/Al = 1. EFAl leads to an increase in LAS, which in some cases was shown to have a beneficial effect on catalyst lifetime [42], while $Al_2(MoO_4)_3$ was generally agreed to be inactive for MDA [37,43,44]. At the same time BAS are removed leading to a lower acidity, which was shown to decrease the formation of coke [10–14]. Generally, extraction of Al from the framework leads to a decrease in crystallinity, because some microporous structures are destroyed. This can also result in mesoporosity as observed in the N_2 adsorption measurements. Some mesoporosity can be beneficial for the reaction, but there seems to be an optimum of how many mesopores should exist [16,45–47]. Finally, catalytic performance varies more at higher loadings (compare Figs. S2 and S3), also because it becomes harder to disperse Mo.

3.2. Effect of dispersion

3.2.1. Measuring dispersion

A combination of Py IR, XPS and UV–vis is used to elucidate the nature of Mo species present on the catalysts after synthesis. Py IR indirectly probes the amount of cationic sites of Mo inside the pores of the zeolite particles, XPS only probes the outer surface of the zeolite and UV–vis is a bulk technique giving an average of all Mo species present on the catalyst. Thus a combination of all three techniques is insightful for distinguishing between bigger clusters of Mo on the outer surface of the zeolite particle and Mo anchored inside the pores.

Py IR was used to determine how many active Mo sites are created. Fig. 1a, Figs. S11b and S12b show the absorbance bands of pyridine adsorbed on the acid sites of the bare zeolite and the catalysts containing Mo. Three contributions are observed corresponding to Lewis acid sites (LAS) at 1455 cm^{-1}, a mixture of LAS and BAS at 1490 cm^{-1} and BAS at 1546 cm^{-1} [48–50]. In addition, several absorbances are observed between 1612 and 1635 cm^{-1} that represent a mixture of LAS and BAS as well. The intensity for the BAS absorbance at 1546 cm^{-1} decreases for the catalysts with Mo, because the Mo cations replace the acidic protons [21]. Through this exchange new Lewis acid sites are created. One of the absorbances around 1635 cm^{-1} decreases together with the BAS absorbance at 1546 cm^{-1} and is therefore assigned to BASs. Both the absorbance at 1623 cm^{-1} as well as at 1612 cm^{-1} are assigned to LASs. For the bare zeolite, LASs stem from extra-framework Al (EFAl), while on the zeolite containing Mo both LASs from EFAl and from Mo cations are observed. The absorbance at 1612 cm^{-1} only appears for the zeolite containing Mo, therefore this wavenumber is assigned to LAS arising from Mo cations while the absorbance at 1623 cm^{-1} likely stems from EFAl [21]. Comparing Figs. S11a and S12a, it can be seen that for Mo/Al = 1, the OH absorbance corresponding to Si−OH and Al−OH almost disappeared. This is because Mo is also anchored on those groups for high loadings. A complete table containing the fraction of BAS covered and the amount of extra LAS created for each sample can be found in the SI (Table S1). In Fig. 1b, the amount of additional LASs created, LAS_{extra} is plotted against the ratio of BAS covered, $(Mo/Al)_{Py\ FTIR}$. Proportionally the more LASs are created, the more acidic protons are replaced by Mo cations. Some EFAl is created during the synthesis of the zeolite, likely during the calcination step, as discussed in the SI, section A3. This explains why the bare zeolite, **HZ** does not follow the same linear trend as the other samples. The catalysts with Mo however, follow one trend, because the amount

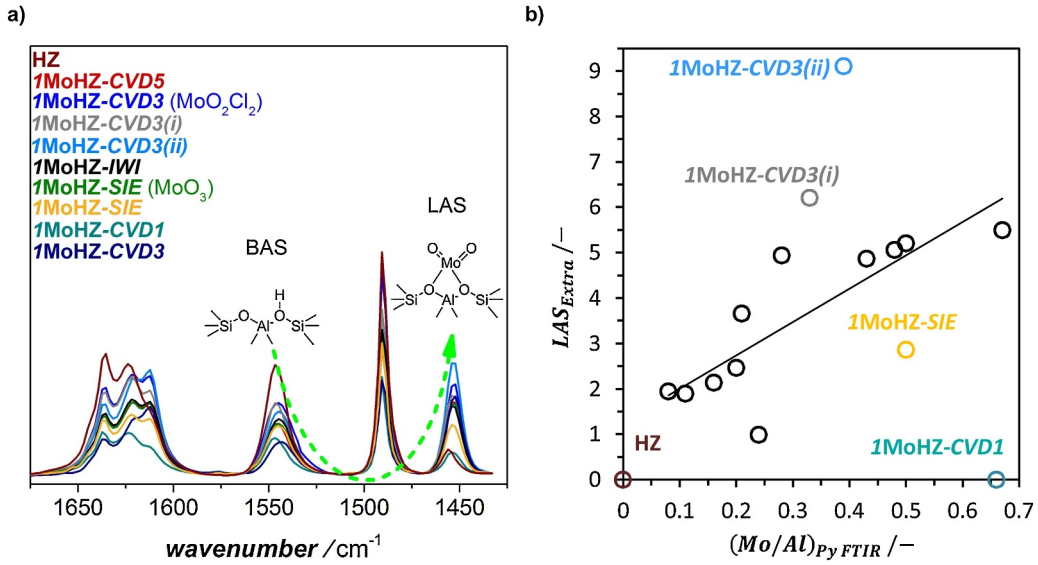

Fig. 1. a) Py IR spectra of *1*MoHZ-*x* samples with illustration of how the Mo cation replaces the proton at the BAS to create LAS. b) $\boldsymbol{LAS_{extra}}$ as determined by integrating the absorbance at the IR wavenumber characteristic for pyridine adsorption on LAS and subtracting the area of the absorbance at the same location on the bare zeolite plotted against $\boldsymbol{(Mo/Al)_{Py\ FTIR}}$ as determined by integrating the absorbance at the IR wavenumber characteristic for pyridine adsorption on BAS for a sample containing Mo and comparing it to the area of the same absorbance measured for the bare zeolite. Results for all samples are plotted and outliers highlighted. For all values refer to Table S1.

of EFAl created is similar for most samples as shown by ^{27}Al MAS NMR in Fig. S10. ***1*MoHZ-*CVD1*** presents an outlier, as no extra LASs are created in that case during the incorporation of Mo. This indicates that most of the decrease in the characteristic BAS absorbance is not because Mo replaced the acidic proton, but because the BASs got destroyed during the synthesis. Similarly for ***1*MoHZ-*SIE*** the decrease in BAS is partly due to extraction of FAl and formation $Al_2(MoO_4)_3$. In contrast, for ***1*MoHZ-*CVD3(i)*** and ***1*MoHZ-*CVD3(ii)***, more EFAl was created during the synthesis compared to other samples.

Since XPS is a surface sensitive technique, which for our specific experimental configuration has a mean escape depth of around 3–4 nm (details in SI section A5.5) [51–53], it can inform about agglomeration and clustering of Mo on the external surface of the catalyst particles. An agglomeration on the outer surface of the zeolite crystal will yield an increased amount of Mo detected by XPS. XPS confirms that Mo does not significantly cluster on the outer surface of the catalyst particle for catalysts synthesized with Mo/Al = 0.3, as the Mo/Al ratios obtained from XPS for those samples are all below 0.33, while they can be as high as 1.44 for catalysts synthesized with Mo/Al = 1 (Table S1). The more Mo anchors to the BAS, the less Mo is expected to be present as bigger clusters and nanoparticles on the outer surface of the zeolite and the lower the expected $\boldsymbol{(Mo/Al)_{XPS}}$. Indeed, a decrease in the Mo/Al ratio obtained from XPS with Mo/Al ratio determined by Py IR is observed for the same Mo loading (Fig. 2a). The $\boldsymbol{(Mo/Al)_{XPS}}$ was determined as

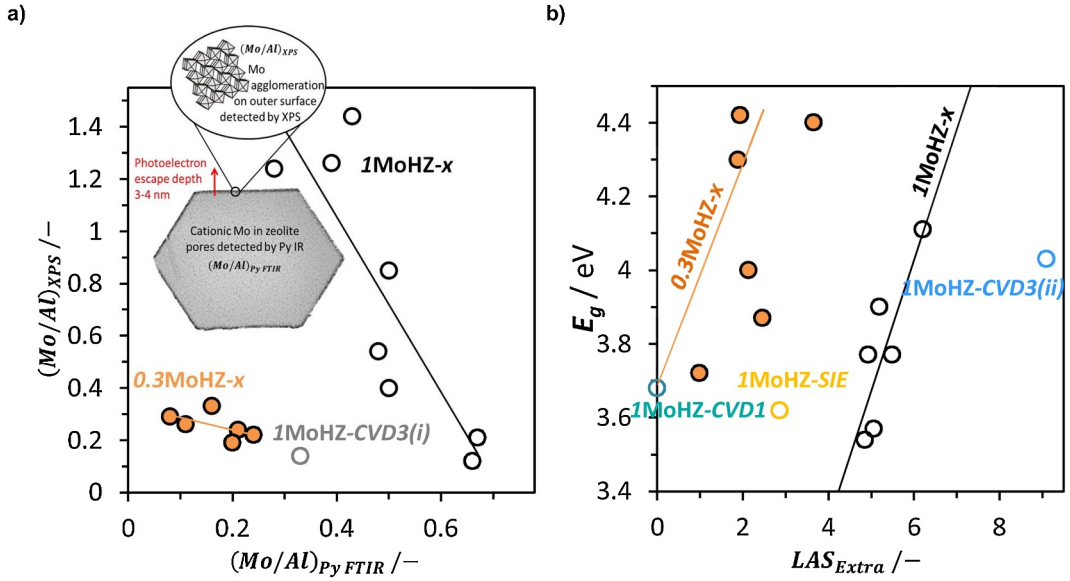

Fig. 2. a) $\boldsymbol{(Mo/Al)_{XPS}}$ on the outer surface of the catalyst particle as determined by quantifying the amount of Mo and Al from the XPS measurement plotted against $\boldsymbol{(Mo/Al)_{Py\ FTIR}}$ as determined by integrating the absorbance at the IR wavenumber characteristic for pyridine adsorption on BAS for a sample containing Mo to the same absorbance measured for the bare zeolite. Results for all samples are plotted and outliers highlighted. For all values refer to Table S1. b) Edge energy E_g determined from UV–vis (Fig. S19, Table S1) plotted against $\boldsymbol{LAS_{extra}}$ as determined by integrating the absorbance at the IR wavenumber characteristic for pyridine adsorption on LAS and subtracting the area of the absorbance at the same location on the bare zeolite.

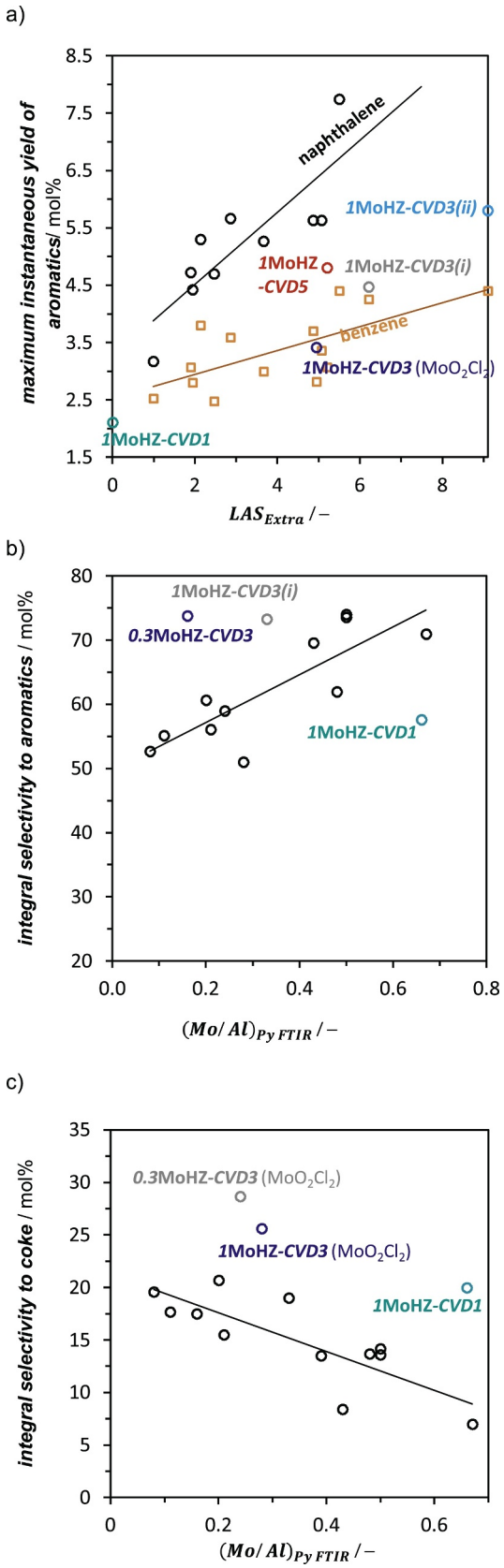

Fig. 3. a) Instantaneous maximum yield to benzene and naphthalene (Table S3). b) The integral selectivity to aromatics (Table S2) plotted against the ratio of BAS covered, $(Mo/Al)_{Py\ FTIR}$ (Table S1). c) The integral selectivity to coke (Table S2) plotted against the ratio of BAS covered, $(Mo/Al)_{Py\ FTIR}$ (Table S1).

an average of two measurement locations. These values for the different locations on the same sample can vary considerably at high Mo loadings (Table S1), demonstrating local clustering of Mo on the external surface revealed by the XPS measurement.

UV–vis can be used to determine the electronic edge energy (E_g) of the charge transfer from oxygen to molybdenum. For samples with Mo/Al = 0.3, E_g is generally between 4.00 and 4.42 (Table S1) suggesting that with such low loadings, Mo is almost exclusively present as mono- or dimeric species [27]. For Mo/Al = 1, E_g is generally a bit lower, because this ratio is at the limit of how much Mo can be anchored to the BAS of the zeolite framework and Mo oxide polymers will always be present to some extent. Fig. 2b shows that E_g generally increases with the number of extra Lewis acid sites created compared to the bare zeolite, confirming that these LASs correspond to mono- or dimeric Mo cations. The limitations of using E_g as an indicator of dispersion however are also clear, as many outliers can be found in Fig. 2b. Even worse correlations were found when trying to correlate the results from UV–vis with results from XPS.

3.2.2. Relating dispersion to catalytic activity

Finally, the measure for dispersion $(Mo/Al)_{Py\ FTIR}$ determined with pyridine IR can directly be related to catalytic performance. The overall activity is increased when more well-dispersed cationic Mo sites are created. This is evident from the increase in the instantaneous yield of naphthalene and benzene with $(Mo/Al)_{Py\ FTIR}$ shown in Fig. 3a. More benzene and naphthalene are produced leading to an increased integral selectivity to aromatics (Fig. 3b), and a decreased integrated selectivity to coke (Fig. 3c). ***1*MoHZ-*CVD1*** presents an outlier in all three relationships, because of the significant destruction of the zeolite during synthesis as discussed in Section 3.1. The other outliers in the trend for selectivity to aromatics can be explained by the particularly low selectivity to C2–C3 hydrocarbons, effectively increasing aromatics selectivity. The other outliers in Fig. 3c correspond with a prolonged activation period. During the activation period, the oxidic Mo present on the as-synthesized catalysts is carburized to its active phase, which leads to a delay in the onset of aromatics production [54]. This is observed for ***1*MoHZ-*CVD3***(MoO_2Cl_2) and ***0.3*MoHZ-*CVD3***(MoO_2Cl_2) (Fig. S3). This prolonged activation period leads to an increased coke production already in the beginning of the reaction.

Carburization takes longer, because of the presence of bigger Mo particles on ***1*MoHZ-*CVD3***(MoO_2Cl_2) and ***0.3*MoHZ-*CVD3***(MoO_2Cl_2), which are observed as MoO_3 diffraction peaks in the XRD pattern (Fig. S9) and as a weight increase in the TGA curve right before the onset of coke combustion on the spent catalyst (Fig. S14), which occurs when bigger Mo_2C particles are oxidized (Fig. S15). The ***1*MoHZ-*CVD1*** sample suffered from severe Al extraction from the framework, resulting in structural changes (Fig. S8b) and formation of inactive $Al_2(MoO_4)_3$ (Fig. S10b). Brønsted acidity was therefore reduced considerably and no Lewis acidity created (Fig. S12).

3.3. Effect of acidity and porosity

When exchanging the proton at the BAS with Mo, Mo active sites are created while simultaneously decreasing the acidity [30]. That is why it is difficult to separate the effect of more Mo sites from the effect of lowering the amount of acid sites. Although it has been shown that coke selectivity decreases when the Brønsted acidity of the zeolite is lowered [10–14], this is not the sole reason as might be suggested by Fig. 3c. Additionally, the aromatics formation rate increases, because there are more well-dispersed Mo sites on which methane can be activated (Fig. 3a). As a consequence, it is not enough to create a zeolite support with low acidity to enhance aromatic selectivity as has been suggested [47], but the amount of well-dispersed Mo sites has to be increased as well. This is similar to what has been shown for Ca species for the methanol to olefins reaction [42,48].

We further assessed the effect of porosity on catalytic performance.

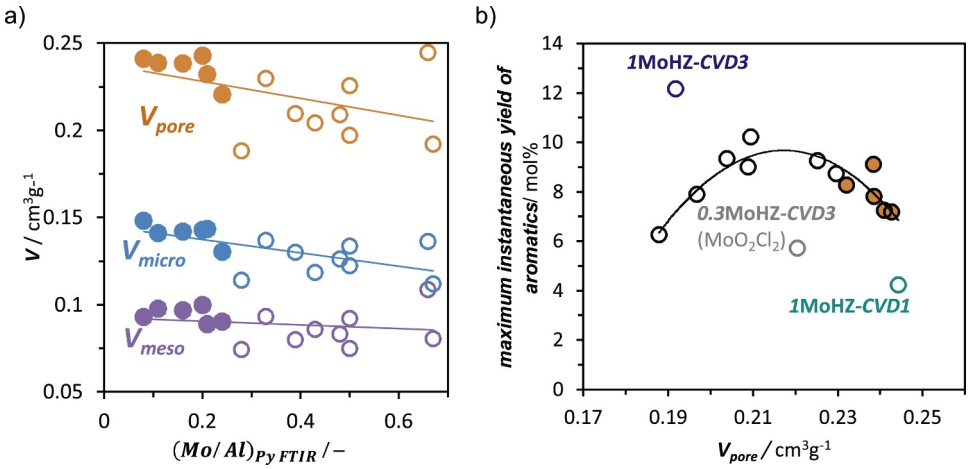

Fig. 4. a) meso- micro- and total pore volume (Table S4) as a function of $(Mo/Al)_{Py\ FTIR}$. Catalysts with Mo/Al = 0.3 are indicated by solid symbols. b) Maximum instantaneous yield to aromatics (Table S2) as a function of total pore volume (Table S4). Samples with Mo/Al = 0.3 are indicated in *orange* (For interpretation of the references to colour in this figure legend, the reader is referred to the web version of this article.).

Pore volume, especially micropore volume decreases with $(Mo/Al)_{Py\ FTIR}$, because more Mo is anchored inside the pores of the zeolite (Fig. 4a). For Mo/Al = 0.3, maximum instantaneous yields to aromatics decrease with pore volume, because more Mo cationic sites are present (orange points, Fig. 4b). In contrast, for a higher loading of Mo, the maximum instantaneous yields to aromatics are higher for higher pore volumes. The rate of aromatics formation for these catalysts with a lot of active Mo sites is very high and thus diffusion of the products starts to impact catalyst performance. A longer catalyst lifetime can also be expected for a higher pore volume, because more coke can be accommodated before access to the active sites of the catalyst is blocked. The total amount of coke deposited after 364 min on stream increases with pore volume (Fig. S16), but this is not due to a complete filling of the pores, since the pore volume of the catalysts decreased by less than 40% during the 364 min on stream and mesopore volume decreased relatively more than micropore volume (Table S6). Total coke amounts instead increase because the concentration of BASs is also higher at higher pore volumes (Fig. 4a). Coke formation is thus clearly associated with acidity. This is supported by the fact that for the catalysts with lower loadings of Mo and thus higher acidity, activity drops around by 70% and only by 30–60% for the high loadings. The drop in benzene formation is also much higher than the decrease in pore volume indicating that coking might not be the only cause of deactivation, but agglomeration of Mo could play a role as well, as has been suggested before [17,55]. The integrated aromatic selectivities follow a similar trend as the maximum instantaneous yields (Fig. S17), demonstrating that more cationic Mo sites increase activity at low Mo loadings and that it is important to increase accessibility for high Mo loadings.

4. Conclusions

Comparing and adapting several CVD techniques from literature and using the conventional preparation techniques, IWI and SIE, a suite of 17 catalysts were synthesized, characterized and their catalytic performance tested for MDA. The synthesis method had a greater effect on catalyst performance for the high Mo loading corresponding to a Mo/Al ratio of 1, while the different synthesis methods lead to more similar performance for Mo/Al = 0.3. Mo/Al = 1, which corresponds to a loading of 5.8 wt.% Mo on a zeolite with Si/Al = 25, represents the theoretical maximum of Mo that can be anchored to the framework Al of the zeolite. At this loading, dispersing Mo while avoiding the formation of Mo nanoparticles is difficult to achieve. Full exchange of the acidic protons with Mo is controlled by migration of the Mo precursor into the pores of the zeolite. This migration can be enhanced by using a Mo precursor with a lower melting point.

Characterization with pyridine IR, XPS, UV–vis and ^{27}Al MAS NMR allowed determining the amount of Mo present as mono- or dimeric species inside the pores of the zeolite as well as the fraction of Mo that formed nanoparticles and bigger clusters on the outer surface of the zeolite. Py IR showed to be the most informative technique in that regard, as XPS shows a high local measurement variation, and edge energies determined from UV–vis do not correlate well with results from other characterization techniques. The information from Py IR can be related well with catalytic behavior. A linear relationship was found between the rate of aromatics formation (benzene and naphthalene) and the concentration of Mo cations inside the channels of HZSM-5. Hence, when more Mo cations are present the integral selectivity to aromatics also increases and at the same time the selectivity to coke decreases due to a simultaneously reduced acidity.

Both the dispersion of Mo as well as overall acidity influence catalytic performance. Thus, it is not sufficient to create a zeolite support with low acidity to enhance aromatic selectivity as has been suggested [47], the amount of well-dispersed Mo sites has to be increased as well. Coking can clearly be associated with the acid sites. In addition, bigger Mo nanoparticles prolong the induction period and the catalyst deactivates faster. Deactivation also occurs because of agglomeration of Mo and thus a decrease in the number of cationic Mo sites. The number of cationic Mo-sites is the most important factor determining the activity of Mo/HZSM-5 for low loadings of Mo, but at higher loadings, catalysts design should also provide for enough porosity to enhance diffusion of products.

Declaration of interest

We declare no conflict of interest.

Funding

This work was supported by the Nederlandse Organisatie voor Wetenschappelijk Onderzoek [731.014.302].

Acknowledgements

Financial support from the Sabic-NWO CATC1CHEM CHIPP project is gratefully acknowledged. Thanks go to Dr. Christoph Dittrich (SABIC), Dr. Frank Mostert (SABIC) and Dr. T. Alexander Nijhuis (SABIC) for fruitful discussion.

Appendix A. Supplementary data

Supplementary material related to this article can be found, in the online version, at doi:https://doi.org/10.1016/j.apcata.2019.01.022.

References

[1] N.E.T. Laboratory, An Introduction to the Science and Energy Potential of a Unique Resource, US Department of Energy, US, 2011.
[2] B.S. Liu, L. Jiang, H. Sun, C.T. Au, Appl. Surf. Sci. 253 (2007) 5092–5100.
[3] K. Honda, X. Chen, Z.-G. Zhang, Catal. Commun. 5 (2004) 557–561.
[4] Y. Song, Y. Xu, Y. Suzuki, H. Nakagome, Z.-G. Zhang, Appl. Catal. A Gen. 482 (2014) 387–396.
[5] Y. Xu, L. Lin, Appl. Catal. A Gen. 188 (1999) 53–67.
[6] J.J. Spivey, G. Hutchings, Chem. Soc. Rev. 43 (2014) 792–803.
[7] Z.R. Ismagilov, E.V. Matus, L.T. Tsikoza, Energy Environ. Sci. 1 (2008) 526–541.
[8] Y. Xu, X. Bao, L. Lin, J. Catal. 216 (2003) 386–395.
[9] S. Majhi, P. Mohanty, H. Wang, K.K. Pant, J. Energy Chem. 22 (2013) 543–554.
[10] J.-P. Tessonnier, B. Louis, S. Rigolet, M.J. Ledoux, C. Pham-Huu, Appl. Catal. A Gen. 336 (2008) 79–88.
[11] P. Schwach, X. Pan, X. Bao, Chem. Rev. 117 (2017) 8497–8520.
[12] S. Ma, X. Guo, L. Zhao, S. Scott, X. Bao, J. Energy Chem. 22 (2013) 1–20.
[13] H. Liu, Y. Li, W. Shen, X. Bao, Y. Xu, Catal. Today 93–95 (2004) 65–73.
[14] F. Denardin, O.W. Perez-Lopez, Fuel 236 (2019) 1293–1300.
[15] A. Martínez, E. Peris, M. Derewinski, A. Burkat-Dulak, Catal. Today 169 (2011) 75–84.
[16] D. Ma, Y. Lu, L. Su, Z. Xu, Z. Tian, Y. Xu, L. Lin, X. Bao, J. Phys. Chem. B 106 (2002) 8524–8530.
[17] J. Gao, Y. Zheng, J.-M. Jehng, Y. Tang, I.E. Wachs, S.G. Podkolzin, Science 348 (2015) 686–690.
[18] J.-P. Tessonnier, B. Louis, S. Walspurger, J. Sommer, M.-J. Ledoux, C. Pham-Huu, J. Phys. Chem. B 110 (2006) 10390–10395.
[19] N. Kosinov, A.S.G. Wijpkema, E. Uslamin, R. Rohling, F.J.A.G. Coumans, B. Mezari, A. Parastaev, A.S. Poryvaev, M.V. Fedin, E.A. Pidko, E.J.M. Hensen, Angew. Chem. 57 (2018) 1016–1020.
[20] W. Ding, G.D. Meitzner, D.O. Marler, E. Iglesia, J. Phys. Chem. B 105 (2001) 3928–3936.
[21] I. Vollmer, G. Li, I. Yarulina, N. Kosinov, E.J. Hensen, K. Houben, D. Mance, M. Baldus, J. Gascon, F. Kapteijn, Catal. Sci. Technol. 8 (2018) 916–922.
[22] L.Y. Chen, L.W. Lin, Z.S. Xu, X.S. Li, T. Zhang, J. Catal. 157 (1995) 190–200.
[23] Y. Xu, S. Liu, X. Guo, L. Wang, M. Xie, Catal Lett 30 (1994) 135–149.
[24] J. Shu, A. Adnot, B.P.A. Grandjean, Ind. Eng. Chem. Res. 38 (1999) 3860–3867.
[25] P.L. Tan, C.T. Au, S.Y. Lai, Appl. Catal. A Gen. 324 (2007) 36–41.
[26] T.H. Lim, K. Nam, I.K. Song, K.-Y. Lee, D.H. Kim, Appl. Catal. A Gen. 552 (2018) 11–20.
[27] H. Tian, C.A. Roberts, I.E. Wachs, J. Phys. Chem. C 114 (2010) 14110–14120.
[28] Y.-H. Kim, R.W. Borry, E. Iglesia, Microporous Mesoporous Mater. 35 (2000) 495–509.
[29] D. Ma, Y. Shu, W. Zhang, X. Han, Y. Xu, X. Bao, Angew. Chem. Int. Ed. 39 (2000) 2928–2931.
[30] D. Ma, W. Zhang, Y. Shu, X. Liu, Y. Xu, X. Bao, Catal. Lett. 66 (2000) 155–160.
[31] D. Ma, Y. Shu, X. Han, X. Liu, Y. Xu, X. Bao, J. Phys. Chem. B 105 (2001) 1786–1793.
[32] W. Zhang, D. Ma, X. Han, X. Liu, X. Bao, X. Guo, X. Wang, J. Catal. 188 (1999) 393–402.
[33] B.S. Liu, Y. Zhang, J.F. Liu, M. Tian, F.M. Zhang, C.T. Au, A.S.C. Cheung, J. Phys. Chem. C 115 (2011) 16954–16962.
[34] Y. Shu, D. Ma, L. Xu, Y. Xu, X. Bao, Catal. Lett. 70 (2000) 67–73.
[35] B. Rhimi, M. Mhamdi, V.N. Kalevaru, A. Martin, RSC Adv. 6 (2016) 65866–65878.
[36] S. Liu, L. Wang, R. Ohnishi, M. Ichikawa, J. Catal. 181 (1999) 175–188.
[37] N. Kosinov, F.J. Coumans, G. Li, E. Uslamin, B. Mezari, A.S. Wijpkema, E.A. Pidko, E.J. Hensen, J. Catal. 346 (2017) 125–133.
[38] P.L. Tan, Y.L. Leung, S.Y. Lai, C.T. Au, Appl. Catal. A Gen. 228 (2002) 115–125.
[39] I. Lezcano-González, R. Oord, M. Rovezzi, P. Glatzel, S.W. Botchway, B.M. Weckhuysen, A.M. Beale, Angew. Chem. Int. Ed. 55 (2016) 5215–5219.
[40] R.W. Borry, Y.H. Kim, A. Huffsmith, J.A. Reimer, E. Iglesia, J. Phys. Chem. B 103 (1999) 5787–5796.
[41] N. Kosinov, F.J.A.G. Coumans, E.A. Uslamin, A.S.G. Wijpkema, B. Mezari, E.J.M. Hensen, ACS Catal. (2016) 520–529.
[42] I. Yarulina, K. De Wispelaere, S. Bailleul, J. Goetze, M. Radersma, E. Abou-Hamad, I. Vollmer, M. Goesten, B. Mezari, E.J.M. Hensen, J.S. Martínez-Espín, M. Morten, S. Mitchell, J. Perez-Ramirez, U. Olsbye, B.M. Weckhuysen, V. Van Speybroeck, F. Kapteijn, J. Gascon, Nat. Chem. 10 (2018) 804–812.
[43] J.-Z. Zhang, M.A. Long, R.F. Howe, Catal. Today 44 (1998) 293–300.
[44] W. Liu, Y. Xu, S.-T. Wong, L. Wang, J. Qiu, N. Yang, J. Mol. Catal. A Chem. 120 (1997) 257–265.
[45] L. Su, L. Liu, J. Zhuang, H. Wang, Y. Li, W. Shen, Y. Xu, X. Bao, Catal Lett 91 (2003) 155–167.
[46] Y. Wu, L. Emdadi, Z. Wang, W. Fan, D. Liu, Appl. Catal. A Gen. 470 (2014) 344–354.
[47] Y. Lu, D. Ma, Z. Xu, Z. Tian, X. Bao, L. Lin, Chem. Commun. (2001) 2048–2049.
[48] I. Yarulina, S. Bailleul, A. Pustovarenko, J.R. Martinez, K.D. Wispelaere, J. Hajek, B.M. Weckhuysen, K. Houben, M. Baldus, V. Van Speybroeck, F. Kapteijn, J. Gascon, ChemCatChem 8 (2016) 3057–3063.
[49] S. Bordiga, C. Lamberti, F. Bonino, A. Travert, F. Thibault-Starzyk, Chem. Soc. Rev. 44 (2015) 7262–7341.
[50] C.A. Emeis, J. Catal. 141 (1993) 347–354.
[51] C.J. Powell, A. Jablonski, Detectors Assoc. Equip. 601 (2009) 54–65.
[52] A.J.C.J. Powell, NIST Electron Inelastic-Mean-Free-Path Database, Version 1.2, SRD 71, National Institute of Standards and Technology, Gaithersburg, MD, 2010.
[53] J.C. Ashley, V.E. Anderson, J. Electron Spectros. Relat. Phenomena 24 (1981) 127–148.
[54] H. Jiang, L. Wang, W. Cui, Y. Xu, Catal. Lett. 57 (1999) 95–102.
[55] E.V. Matus, I.Z. Ismagilov, O.B. Sukhova, V.I. Zaikovskii, L.T. Tsikoza, Z.R. Ismagilov, J.A. Moulijn, Ind. Eng. Chem. Res. 46 (2007) 4063–4074.